Journal of The Electrochemical Society

The Surface Cell Cooling Coefficient: A Standard to Define Heat Rejection from Lithium Ion Battery Pouch Cells

Journal of The Electrochemical Society, 2020 **167** 020524

The Surface Cell Cooling Coefficient: A Standard to Define Heat Rejection from Lithium Ion Battery Pouch Cells

Alastair Hales,[1] Mohamed Waseem Marzook,[1] Laura Bravo Diaz,[1] Yatish Patel,[1] and Gregory Offer[1,2,*,z]

[1]*Department of Mechanical Engineering, Imperial College London, London SW7 2AZ, United Kingdom*
[2]*The Faraday Institution, Quad One, Harwell Science and Innovation Campus, Didcot, United Kingdom*

There is no universal and quantifiable standard to compare a given cell model's capability to reject heat. The consequence of this is suboptimal cell designs because cell manufacturers do not have a metric to optimise. The Cell Cooling Coefficient for pouch cell tab cooling (CCC_{tabs}) defines a cell's capability to reject heat from its tabs. However, surface cooling remains the thermal management approach of choice for automotive and other high-power applications. This study introduces a surface Cell Cooling Coefficient, CCC_{surf} which is shown to be a fundamental property of a lithium-ion cell. CCC_{surf} is found to be considerably larger than CCC_{tabs}, and this is a trend anticipated for every pouch cell currently commercially available. However, surface cooling induces layer-to-layer nonuniformity which is strongly linked to reduced cell performance and reduced cell lifetime. Thus, the Cell Cooling Coefficient enables quantitative comparison of each cooling method. Further, a method is presented for using the Cell Cooling Coefficients to inform the optimal design of a battery pack thermal management system. In this manner, implementation of the Cell Cooling Coefficient can transform the industry, by minimising the requirement for computationally expensive modelling or time consuming experiments in the early stages of battery-pack design.

 [DOI: 10.1149/1945-7111/ab6985]

Manuscript submitted October 25, 2019; revised manuscript received December 28, 2019. Published January 22, 2020.

List of symbols

A	Surface area, m^2
C_{th}	Thermal conductance, $W.K^{-1}$
CCC	Cell Cooling Coefficient, $W.K^{-1}$
I	Current, A
I_{pulse}	Magnitude of current used during pulsing cycle, A
k	Thermal conductivity, $W.m^{-1}K^{-1}$
k_{eff}	Effective thermal conductivity, $W.m^{-1}K^{-1}$
$\dot{Q}$	Heat rate, W
$\dot{Q}_{gen}$	Cell heat generation rate, W
R	Resistance, Ω
R_{int}	Cell internal equivalent resistance (Ω)
t	Time, s
T	Temperature, °C
T_{con}	Control temperature, °C
ΔT_{cell}	Temperature difference across a cell, induced by a cooling mechanism, °C
U_{OC}	Cell open circuit potential (V)
V	Cell potential (V)
x	Thickness, m
α_{loss}	Heat rate loss fraction, [dmls]

Subscripts

cables	Value relevant to the cell cycler cables
clamps	Value relevant to the tab clamps
f i	Value relevant to fin i
neg	Value relevant to negative tab
pos	Value relevant to positive tab
surf	Value relevant to surface cooling
tabs	Value relevant to tab cooling

Lithium-ion batteries (LIBs) have become the dominant technology for sustainable energy storage in recent years.[1] LIB uptake is increasing rapidly in many fields of industry and aspects of society, due to the climate crisis caused by greenhouse gas emissions, major health concerns regarding air quality, and a requirement for energy security into the future.[2,3]

Thermal management is a critical concern because LIBs generate a considerable amount of heat during operation, particularly for demanding application such as in the automotive industry.[4–10] This heat is generated due to the electrochemical processes occurring at the pore-scale in LIBs.[4,9,11–16] Reversible heat is generated due to the material phase changes and therefore entropy change. Irreversible heat is caused by the so-called ohmic heat related to long-range interactions (transport of charge and species in the electrolyte and solid phases) and the kinetic heat related to short-range interactions (charge-transfer reactions at the interphase).[16] The heat generation rate by a single cell can be described generally by Eq. 1.[7]

$$\dot{Q} = I \cdot (U_{OC} - V) - I \cdot \left(T \cdot \frac{dU_{OC}}{dT}\right) = R \cdot I^2 - I \cdot \left(T \cdot \frac{dU_{OC}}{dT}\right) \quad [1]$$

The first term represents the irreversible heat, considering the charge transfer overpotential at the interface, ohmic heat, kinetic heat and mass transfer limitations. The second term accounts for the reversible entropic heat. The first term may be expressed as $R_{int} \cdot I^2$ where R_{int} is the internal equivalent resistance of the cell (Ω).

Cell impedance is a strong function of temperature. Inhomogeneous impedance across a pack leads to uneven current distributions during operation, demonstrated to increase the rate of degradation.[12,17–20] Additionally, cells must operate below a specified maximum temperature to mitigate the risk of thermal runaway.[21,22] As a result, an essential function of a battery management system (BMS) is to control the thermal management system (TMS). The TMS aims to maintain an optimum temperature range for each cell in a pack, and the degree to which this is achieved is therefore a result of how effective the TMS is at cooling, and at cooling each cell equally.

TMSs employ either liquid or air cooling mechanisms in the vast majority of battery packs. Air cooling is now restricted to low-discharge rate applications, due to the increase in achievable energy density and power capability of modern cells, and therefore the increase in their volumetric heat generation rate.[23,24] Liquid cooling

*Electrochemical Society Member.
[z]E-mail: gregory.offer@imperial.ac.uk

may be implemented through indirect (e.g. heat plates) or direct (e.g. immersive) cooling on a particular surface of a cell, or in combination with the use of phase-change materials.[25–29] Specially designed pouch cells may be thermally managed through their tabs in exceptional cases. For automotive applications, however, surface cooling is typically the only viable method for achieving the required heat rejection rates from the cell.[25,28–31] The cell is almost always cooled on a single surface, allowing two cells to be stacked adjacent to one another in a battery pack.[32,33] The heat generated within a cell is transferred through conduction over a characteristic length within the cell volume, to the cooled surface.[34,35]

Heat transfer requires thermal gradients, therefore a TMS and BMS working together cannot entirely eliminate thermal gradients within cells, regardless of cooling strategy.[20,36,37] Cell-level thermal gradients, brought on by a given rate of heat generation within a cell, may be approximated through numerical analysis. This is impractical in application. Each geometric and thermal parameter within a cell must be accounted for. This requires complex models and complete knowledge of the cell's internal characteristics.[24,38,39] Table I reports the internal geometric and thermal characteristics that affect the thermal gradient induced by surface cooling of two commercially available Kokam pouch cells: SLPB11543140H5, a high-power 5 Ah cell (LIB A) and SLPB75106100, an energy 7.5 Ah cell (LIB B).[20,40] Additionally, the theoretical effective thermal conductivity, k_{eff}, for heat transfer normal to the layer-plane has been calculated. The presented thermal characteristics were determined for each material when wetted, i.e. electrolyte was present.[41] However, the theoretically derived values may be inaccurate because there are unaccountable unknowns. For example, the thermal resistance attributed to each of the many hundred material interfaces within the cell, the effect of any adhesives used to hold the electrode-stack together within the pouch, or the degree to which the thermally conductive pouch material provides a heat rejection pathway for each layer.[37,42,43]

Table II reports the measurable external dimensions of LIB A and LIB B. The surface area for conductive heat transfer associated with surface cooling is 4680 mm^2 and 9084 mm^2 respectively. Therefore, the heat flux per unit of conductive heat rate would be 94.1% greater for LIB A. Further to this, LIB A has a 52.7% greater thickness, which increases the average characteristic length over which heat transfer must occur for surface cooling. The effect of the geometric variation on cell thermal performance is unquantifiable because heat is generated nonuniformly within a cell. Localised heat generation rate is a function of multiple operational parameters including temperature, current magnitude, state-of-charge (SOC), state-of-health (SOH) and drive cycle profile.[7,8,10,44,45]

Certain metrics are well established to quantify the thermal performance of a given body. The Biot number and thermal conductance for a lumped body have both been used in the lithium-ion cell research field.[46,47] They require the assumption that all heat is conducted from one plane of a body to another. This is not the case for cells used in vigorous cycle applications, because heat generation is distributed nonuniformly throughout a cell's volume.[34] Further, both measures require a value for the thermal conductivity of the cell. This may be theoretically approximated if material properties are known. The accuracy of this method, however, cannot be quantified because of the unknown effects of the casing and electrode-stack interfaces. Empirical calculation is possible but often impractical given the significant work required.[20,43]

In response to similar problems when calculating the effectiveness of tab cooling, previous work has introduced a metric and a standardised method to empirically quantify tab cooling performance for pouch cells.[42] This was driven by a necessity to assess the feasibility, in terms of heat removal rate, for a given cell in a given application. The heat rate through the cooled tabs, $\dot{Q}_{tabs}$, is compared against the thermal gradient from the cell's maximum to the tab temperature, ΔT_{cell}, as a ratio. The tab Cell Cooling Coefficient, CCC_{tabs}, is found through Eq. 2.

$$CCC_{tabs} = \frac{\dot{Q}_{tabs}}{\Delta T_{cell}} \quad [2]$$

In the previous work,[42] a bespoke experimental apparatus was constructed which included 220 mm long brass busbars connecting each cell tab to a *Bio-logic* cell cycler. The busbars also provided a thermal pathway for tab cooling of the pouch cell, from the cell tabs to a heat sink mounted at the other end of the busbar. This heat sink was maintained at a constant temperature throughout testing. Two thermocouples on each busbar monitored the thermal gradient along each and, through knowing the material properties and geometric dimensions of the busbars, these magnitudes were used to evaluate the rate of heat rejection from each cell tab to the heat sink, $\dot{Q}_{neg} + \dot{Q}_{pos} = \dot{Q}_{tabs}$. ΔT_{cell} (Eq. 2) refers to the temperature difference from the cell maximum temperature and the average of the tab temperatures. The tab temperatures were found through thermocouples mounted in the tab clamps (identical clamps were used in the present study, see the Experimental section). The cell maximum temperature was found also using thermocouples. The placement of these thermocouples was based on results taken from a numerical model.[37]

The cell-wide heat generation distribution that would occur in a real-world application can only be induced in a lithium-ion cell by passing current through the cell. The CCC determination process uses a square wave pulse drive cycle, with $I_{average} = 0$ A to maintain a constant SOC, to continuously pass current through the cell. In doing so, the induced heat generation distribution replicates that of a real-world application. Evaluation of a given cell's thermal performance using this method bypasses the unjustifiable assumptions required to calculate the Biot number and the thermal conductance of the cell. CCC_{tabs} was demonstrated to be a singular value for a given cell model at beginning of life, independent of operating temperature and heat generation rate.

This investigation developed the surface Cell Cooling Coefficient, CCC_{surf}. In the study, we have demonstrated that the same principle of cell performance assessment, described in previous work,[42] may be used to quantify the thermal performance of a surface cooled cell. The second objective was to use CCC_{surf} and CCC_{tabs} to compare surface cooling to tab cooling for LIB A and LIB B, and to determine each cell's suitability for an example battery pack application where either surface or tab cooling may be applied.

In this paper, we show the CCC_{surf} to be a valuable tool for battery pack designers, to specify the TMS requirements far earlier in the design process than otherwise. As a result, the metric can be used to down-select the cell most suitable for a specific application. The CCC_{surf} can also be used to assess pack-wide thermal gradients without the requirement of complex numerical methods, and therefore can inform thermally coupled degradation models to improve lifetime and estimate performance. Finally, in addition to energy density and capacity, the CCC_{surf} is a metric that cell manufacturers can use for cell design optimisation and to compete against one another. This will improve the performance and lifetime of the next generation of cells.

Experimental

Apparatus.—The two Kokam pouch cells termed LIB A and LIB B[42] were used in this study. LIB A has a $LiMnNiCoO_2$ (NCM) cathode, whilst the cathode for LIB B is $Li(Ni_{0.4}Co_{0.6})O_2$. The anode is graphite in both. All cells used in this investigation were new and at beginning of life. The same two cell models were used to investigate CCC_{tabs} in previous work[42] to enable a comparison between surface and tab cooling.

A schematic of the experimental apparatus used for LIB A is shown in Fig. 1. The setup for LIB B is conceptually identical. The cell is mounted between brass clamps and sat within the bottom insulation shell. A K-type thermocouple (TC7 and TC8) was

Table I. Internal geometric and thermal characteristics, relevant to surface cooling, of LIB A and LIB B. NB: the Separator, anode and cathode were wetted with electrolyte for the calculation of their thermal conductivities[20,40,41]

Component	Negative Current Collector	Positive Current Collector	Separator (wetted)	Anode electrode (wetted)	Cathode electrode (wetted)	Casing
LIB A: Calculated layer-to-layer k_{eff}: 0.916 $W.m^{-1}K^{-1}$						
k/ $W.m^{-1}K^{-1}$	398	238	0.34	1.58	1.04	238
Thickness per layer/ mm	0.0210	0.0210	0.0240	0.0380	0.0290	0.1600
Number of layers	50	51	104	100	100	2
Volumetric proportion of cell	9.38%	9.38%	21.42%	33.93%	25.89%	2.75%
LIB B: Calculated layer-to-layer k_{eff}: 0.645 $W.m^{-1}K^{-1}$						
k/ $W.m^{-1}K^{-1}$	398	238	0.33	1.045	0.44	238
Thickness per layer/ mm	0.0147	0.0151	0.0190	0.0737	0.0545	0.1600
Number of layers	24	25	54	50	50	2
Volumetric proportion of cell	4.53%	4.66%	11.72%	45.46%	33.62%	3.77%

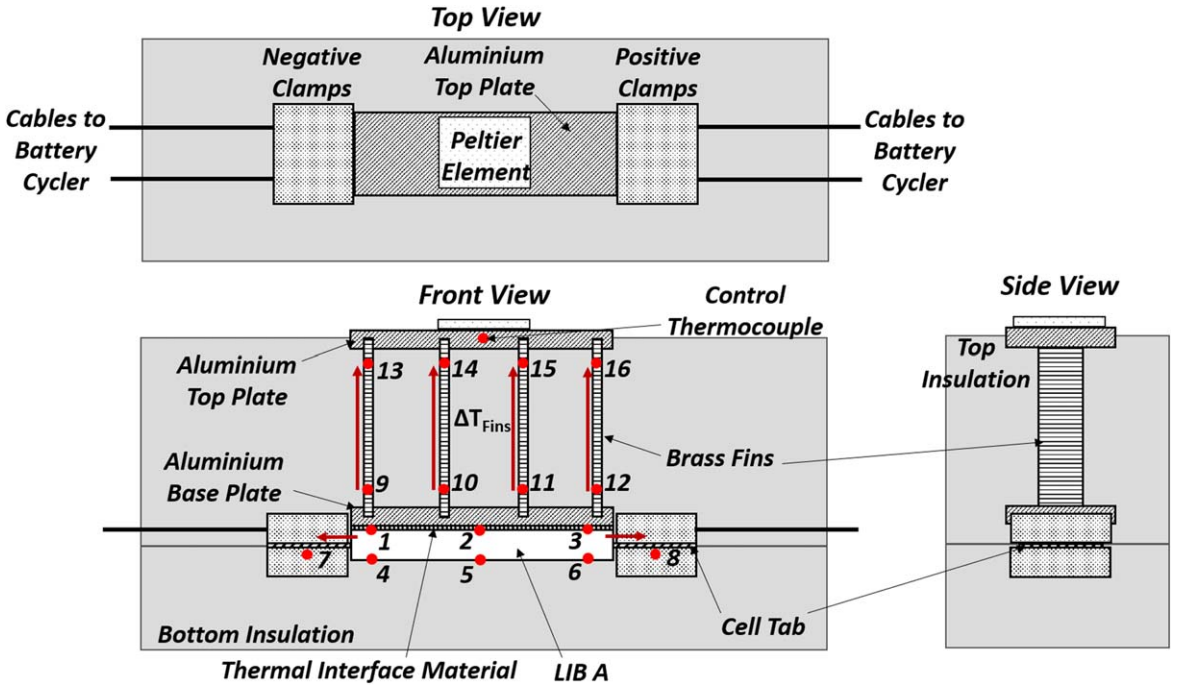

Figure 1. Experimental apparatus setup and thermocouple locations for LIB A.

mounted within each clamp and adhered using thermal epoxy (1.22 $W.m^{-1}K^{-1}$). Unless specifically stated otherwise all following adhered components use this thermal epoxy. The positive and negative connections to the *Bio-logic (BCS 815)* battery cycler (two 1.5 mm^2 insulated copper wires running in parallel, for each tab) were connected to the clamps using ring terminals. The clamps were secured around the tabs using set screws either side, tightened to 12Nm with a torque wrench. This configuration setup was found to minimise electrical resistance, and therefore ohmic heating, within the clamp-tab subassembly. There was also an electrical resistance, and therefore ohmic heat generation, along the length of the parallel copper wires connecting the battery cycler. The conductive dissipation of this heat could not be interpreted accurately because the thermal gradient along the copper cables was difficult to quantify and found to vary from test to test. Therefore, additions are proposed in the Results section to quantify this conductive heat transfer as a function of measurable thermal gradients through the cells' tabs.

LIB A was set up with three thin-leaf k-type TCs (TC1—TC3) placed on the top surface and held in place using thermally conductive kapton tape. TC1—TC3 had a thickness of just 50 μm and a width of 3.2 mm, ensuring they did not reduce the quality of the contact between the cell and the aluminium base plate. The consistency of this interface was further ensured using a layer of 0.5 mm thick thermal interface gel (8 $W.m^{-1}.K^{-1}$). TC4—TC6 adhered to the bottom surface of the cell. The TCs on LIB B were set up as detailed in Fig. 2.

The linear array for TC1—TC3 and TC4—TC6, shown in Fig. 1, provides the optimal coverage of each LIB A surface with three thermocouples. This is because LIB A has a length: width ratio of almost 3:1 (see Table II). LIB B, meanwhile, has a length: width ratio close to 1:1 (see Table II). Therefore, for LIB B, a triangular thermocouple array was preferred, as shown in Fig. 2. Further to this logic, the data interpretation introduced in the Results section requires a cell surface temperature close to the tabs, in order to approximate the rate of heat loss or gain through the tabs. Therefore, for LIB A, TC1 and TC4 must be close to the negative tab, and TC3 and TC6 must be close to the positive tab. Likewise, for LIB B, TC3 and TC6 must be close to the tabs.

TC2 and TC5 were placed close to the tabs because the data interpretation introduced in the Results section requires a cell surface temperature close to the tabs in order to approximate the rate of heat loss or gain through the tabs.

The base plate, 10 mm in thickness, was placed with a pressure of 41.9 kPa on to the top surface of the cell, set using a known mass of 20 kg. Aluminium alloy 6082T6, with a high thermal conductivity (180 $W.m^{-1}K^{-1}$), was used for the base and top plates to ensure a uniform cell surface temperature and uniform heat distribution through the four fins. Thus, the quality of thermal pathway through each brass fin would be similar, thus maximising the uniformity of

Table II. External geometric characteristics, relevant to surface cooling, of LIB A and LIB B

Characteristic	LIB A	LIB B
Electrode-stack length/ mm	117.0	89.5
Electrode-stack width/ mm	40.0	101.5
Cell thickness/ mm	11.3	7.4

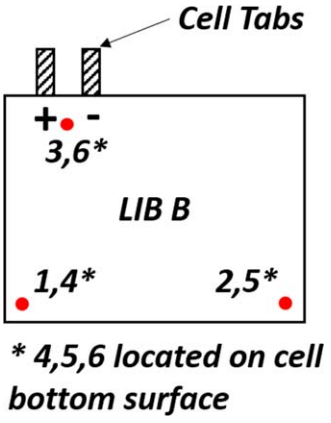

Figure 2. Cell thermocouple locations for LIB B.

Table III. Summary of all tests.

Cell	Number of tests	I_{pulse} range/ A	T_{con} range/ °C
LIB A1	13	7.5–20.0	10.0–25.0
LIB A2	9	7.5–20.0	25.0
LIB A3	5	12.5–20.0	25.0
LIB B1	6	7.5–16.0	20.0

the heat flux rejecting from the cell's cooled surface. The brass fins were adhered into the base and top plate slots. Each fin had a total length of 90 mm, with each cell-side TC (TC9–TC12) located a distance of 65 mm from its corresponding control-side TC (TC13—TC16). This distance was maximised, within reasonable construction constraints, to increase the magnitude of temperature difference between each TC pair and therefore reduce the error due to temperature measurement resolution. Each fin sat in a 5 mm slot in the top and base plates. Therefore, the adjacent faces of the top and base plates were 80 mm from one another. The rate of conductive heat transfer along each fin was evaluated individually in preliminary experimentation and a close correlation was established.

Encasing the assembly in insulation (*Celotex CW3000,* 0.023 $W.m^{-1}K^{-1}$) created a purely conductive system bounded by the insulation's exposed faces. The Peltier element (PE), adhered to the top surface of the top plate, was used to set the control temperature, T_{con}, for the conductive system boundary. Unavoidable heat loss through the insulation was accounted for in the data analysis, explained in the Results section. To minimise the variance of insulation losses from test to test, the apparatus was used inside a thermal chamber, also held at T_{con}.

Experimental procedure.—The experimental procedure is based on that detailed in previous work.[42] Following apparatus setup, the cell under test was subjected to a square wave pulsing current profile, with $I_{average} = 0$ so the SOC is kept constant within a narrow range around 50%. This was done over an extended time period (6 h) to allow the cell to reach a steady temperature state, elevated above T_{con}. The OCV was taken at the start and end of each test, at T_{con}, to verify no change to the initial SOC. The full drive cycle is detailed below. It includes a beginning-of-cycle rest period and an end-of-cycle cell characterisation procedure, to ensure no measurable degradation was occurring between tests. The temperature of each TC, critical for the subsequent thermal analysis, was logged using an *Omega Picologger TC*-08 datalogger, using calibrated thermocouples with an accuracy of ±0.01 °C, at 1 Hz for the duration of each test.

1. 8 h rest to ensure thermal equilibrium at T_{con} across all apparatus
2. Square wave current pulsing at 1 Hz, centred around zero and with test specific current magnitude, for 6 h
3. 2 h rest to reach consistent thermal conditions prior to degradation analysis
4. 1C CC-CV charge to 4.2 V with a 500 mA cut-off, followed by 1 h rest
5. 1C CC discharge to 2.7 V for degradation analysis, followed by 1 h rest
6. 1C CC-CV charge to 4.2 V with 500 mA cut-off, followed by 1 h rest
7. 1C discharge to 50% SOC, followed by a 2 h rest

A total of 33 tests were conducted on four tests cells. I_{pulse} and T_{con} were both varied to induce varying rates of heat generation in the cells under test, and to demonstrate a repeatable methodology for a range of operational conditions. The tests and conditions on each cell are summarised in Table III.

Results

Data interpretation.—The central assumption for the data analysis is that the rate of heat generation within the cell is equal to the rate of heat rejection from the cell when the system reaches a steady temperature state ($\frac{\delta T}{\delta t} = 0$). The mean of the recorded cell surface temperatures (TC1—TC6), $T_{cell\ av}$, was the monitored temperature to determine the region during the pulsing cycle where this assumption was justifiable. Secondly it is assumed that convective heat transfer is negligible within the considered system, i.e. everything enclosed in the insulating material. This was justified because airflow within the system was eliminated, and therefore the surface convective heat transfer coefficients were expected to very low.

The temperature difference across the cell, ΔT_{cell}, from the bottom surface to the top surface, was calculated as the difference in the mean surface temperatures, as set out in Eq. 3.

$$\Delta T_{cell} = \frac{T_{TC4} + T_{TC5} + T_{TC6}}{3} - \frac{T_{TC1} + T_{TC2} + T_{TC3}}{3} \quad [3]$$

The temperature differences from the ends of the cell to the respective tabs, ΔT_{neg} and ΔT_{pos}, was also necessary to account for conductive heat transfer through the cell tabs. Equation 4 shows this for the negative tab, an equivalent was used for the positive tab. The temperature for the negative end of the cell, $T_{cell\ neg}$, was calculated as the mean of the temperatures recorded by TC1 and TC4. The positive end temperature, $T_{cell\ pos}$, was determined from the mean of TC3 and TC6. TC7 and TC8 were used for the negative and positive tab temperatures, $T_{tab\ neg}$ and $T_{tab\ pos}$, respectively.

$$\Delta T_{neg} = T_{cell\ neg} - T_{tab\ neg} \quad [4]$$

For each test, the rate of conductive heat transfer through the top surface of the cell was calculated using TC9—T C16. Equation 5 describes the rate of heat transfer, $\dot{Q}_{f\ 1}$, through fin 1, such that ΔT_{f1} is the tem perature difference between TC9 and TC13. $x_{f\ 1}$ is the distance between TC9 and TC13 (65 mm), A_f is the cross-sectional area of the fin in the plane normal to the direction of conductive heat transfer along its length, and k_f is the thermal conductivity of the fin material (brass grade C121 was used, therefore k_f = 123 $W.m^{-1}K^{-1}$). Equation 6 sums the rate of heat transfer through each fin to output the total rate of conductive heat transfer through the top surface of the cell, $\dot{Q}_{surf}$.

$$\dot{Q}_{f1} = \frac{k_{f1}}{x_{f1}} A_{f1} \Delta T_{f1} \quad [5]$$

$$\dot{Q}_{surf} = \sum_{4}^{n=1} \dot{Q}_{fn} \quad [6]$$

To define the rate of heat transfer for the cell to each tab, the tab CCC values, CCC_{neg} and CCC_{pos}, which are derived in previous work, were used.[42] Consideration of the tab thermal pathways is essential because it is difficult to interpret and quantify the conductive heat transfer in the copper wires connecting the cell to the cycler. Equation 7 defines $\dot{Q}_{neg}$, the rate of heat rejection through the negative tab. $\dot{Q}_{pos}$, the rate of heat rejection through the positive tab, is found in the same manner. The rate of heat addition (due to ohmic heating in the wires and clamp subassemblies), or rate of heat rejection (due to the copper wires providing a pathway for heat conduction away from the cell) is therefore taken into account by simply measuring the thermal gradient from the cell to the respective tab.

$$\dot{Q}_{neg} = CCC_{neg} \Delta T_{neg} \quad [7]$$

The rate of cell heat generation, $\dot{Q}_{gen}$, when in steady temperature state, was calculated by summing the calculated heat transfer rates as in Eq. 8. The portion of generated heat that is rejected through the insulation, and therefore unmeasured by the TCs positioned in the

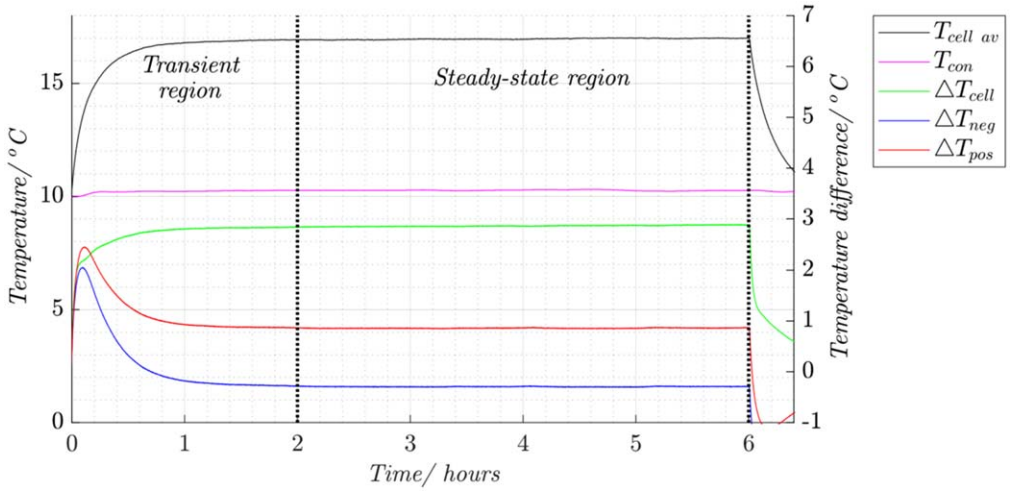

Figure 3. Temperatures and temperature gradients relevant to CCC_{surf} derivation, over the course of the pulsing period for the example dataset (test 1 on LIB A1).

apparatus, is represented by $\dot{Q}_{ins}$.

$$\dot{Q}_{gen} = \dot{Q}_{surf} + \dot{Q}_{neg} + \dot{Q}_{pos} + \dot{Q}_{ins} \quad [8]$$

An apparatus characterisation experiment was conducted to approximate a function for $\dot{Q}_{ins}$, using a resistive heater adhered to the bottom surface of LIB A1 prior to the main set of tests. The procedure was conceptually identical to that in the previous published work.[42] The cell reached an elevated steady temperature state within the insulation when 1.5 W of heat was applied through the resistive heater. 1.419W of heat was recorded leaving the apparatus through monitored pathways ($\dot{Q}_{surf} + \dot{Q}_{neg} + \dot{Q}_{pos}$). It was assumed the remainder, 0.081 W, was rejected directly into the insulation. The loss fraction, α_{loss}, for the LIB A setup was therefore calculated to be 0.054 (5.4% of the heat added to the cell in the characterisation experiment). LIB B's setup produced $\alpha_{loss} = 0.119$. The larger α_{loss} for LIB B may be attributed to the increased surface area of the cell bottom surface, from where the majority of the unaccounted heat is lost. The loss fractions are valid for all cases where the PE temperature and ambient temperature are equal, which was ensured for all tests. $\dot{Q}_{ins}$ may be defined by Eq. 9. Therefore, $\dot{Q}_{gen}$ may be redefined through Eq. 10.

$$\dot{Q}_{ins} = \alpha_{loss}\dot{Q}_{gen} \quad [9]$$

$$\dot{Q}_{gen} = \frac{\dot{Q}_{surf} + \dot{Q}_{neg} + \dot{Q}_{pos}}{1 - \alpha_{loss}} \quad [10]$$

The CCC for a given thermal management process, CCC_i, is defined by Eq. 11, where $\dot{Q}_i$ is the rate of conductive heat transfer through the cooled surface i of a cell and ΔT_{cell} is the temperature difference from the cell maximum to the cooled surface. For the present investigation, $\dot{Q}_{surf}$ represents $\dot{Q}_i$, and therefore the cell cooling coefficient for single surface cooling, CCC_{surf}, is defined by Eq. 12.

$$CCC_i = \frac{\dot{Q}_i}{\Delta T_{cell}} \quad [11]$$

$$CCC_{surf} = \frac{\dot{Q}_{surf}}{\Delta T_{cell}} \quad [12]$$

Data processing.—Figure 3 plots $T_{cell\ av}$ and the control boundary temperature, T_{con}, as well as ΔT_{cell}, ΔT_{neg} and ΔT_{pos}. The annotated steady s tate temperature region is observable. Figure 4 shows $\dot{Q}_{surf}$, $\dot{Q}_{neg}$, $\dot{Q}_{pos}$ and $\dot{Q}_{ins}$, and their sum, $\dot{Q}_{gen}$. The rate of heat rejection through each evaluated pathway is constant in the steady state region. Figure 5 plots CCC_{surf} for the pulsing

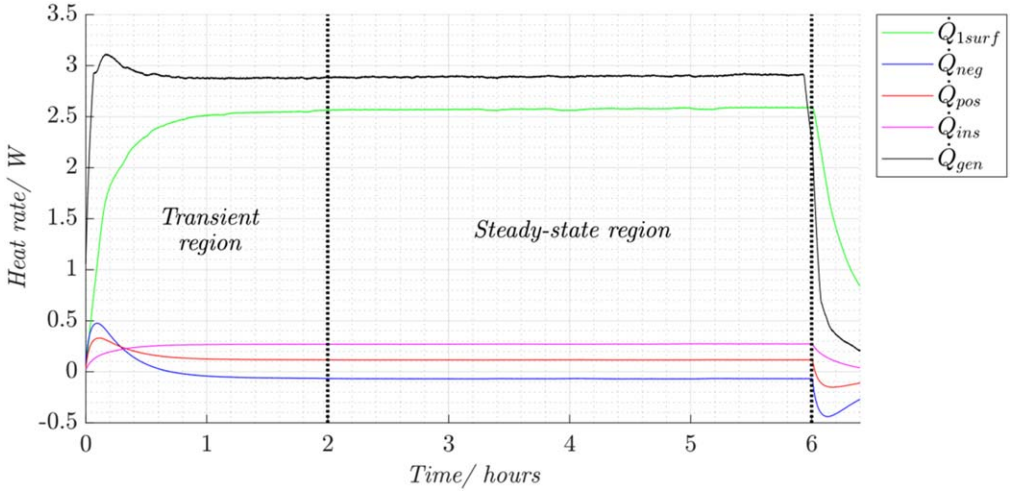

Figure 4. The components of heat rate measurement within the apparatus which sum to equal the derived cell heat generation rate, over the course of the pulsing period for the example dataset (test 1 on LIB A1).

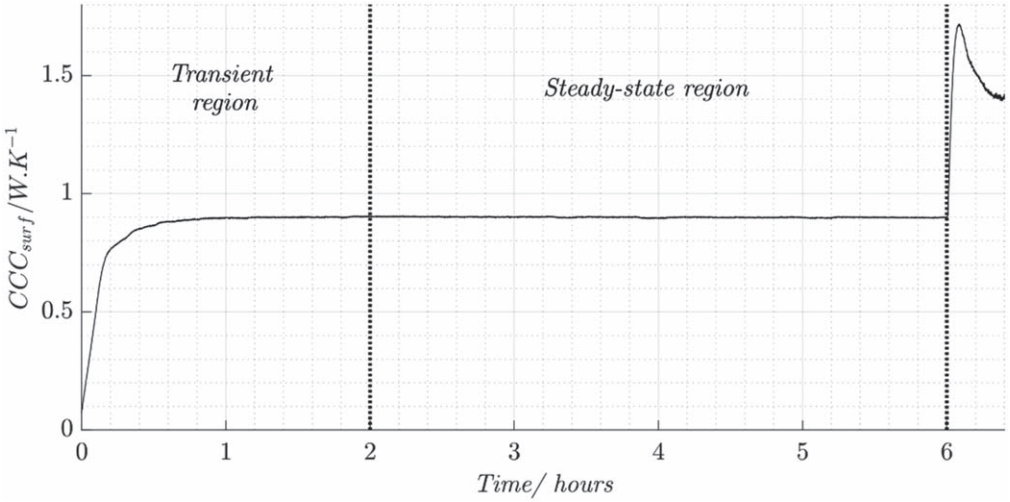

Figure 5. The derived CCC_{surf}, over the course of the pulsing period for the example dataset (test 1 on LIB A1).

cycle. The values for CCC_{surf} appear constant within the steady state region. The mean value across this region is taken forward. In this case, $CCC_{surf} = 0.896$ W.m^{-1}K^{-1}. CCC_{surf} values are not constant away from the steady-state region, because the fundamental assumption required for experimental determination of CCC_{surf}, that heat generation rate within the cell is equal to heat rejection rate from the cell, is unjustified when temperature change occurs with time. The spike following the completion of the pulsing cycle is a clear indicator of where this assumption falls down, and thus highlights the necessity to determine CCC_{surf} in the steady-state region.

Discussion

Justification of results.—The CCC was analysed for tab cooling in previous work and demonstrated to be a singular value for a given cell. The functionality of the CCC_{tabs} derivation process was rigorously tested through experimentation on four cells. I_{pulse} magnitude, T_{con}, and therefore $\dot{Q}_{gen}$, were all varied. The same process to examine the functionality of the CCC_{surf} derivation process was essential in the present study. The inherent variability of the internal resistance associated with the clamp-subassembly will be discussed in detail, and is found to affect the derived CCC_{surf} value for a given cell. In the proceeding analysis, the tests have been split into datasets to best present this effect. These datasets are LIB A1, $T_{con} = 10$ °C, LIB A1, $T_{con} = 25$ °C, LIB A2, $T_{con} = 25$ °C, LIB A3, $T_{con} = 25$ °C, LIB B1, $T_{con} = 25$ °C.

Figure 6 presents CCC_{surf} for every test on cell LIB A, against $\dot{Q}_{surf}$. The vertical error bars summarise the experimental error due to the precision of the temperature measurements, ±0.01 °C. A trend is evident, with greater error in the calculated CCC_{surf} when the magnitude of $\dot{Q}_{surf}$ is smaller. This was expected, because greater $\dot{Q}_{surf}$ corresponds to larger thermal gradients both across the cell and through the brass fins. Therefore, the error due to the absolute temperature precision diminishes as a thermal gradient between any two TCs is increased.

Figure 7 plots the CCC_{surf} error fraction, CCC_{ERR}, against $\dot{Q}_{surf}$ for all tests. This is calculated as the ratio of the temperature measurement error to the derived CCC_{surf} value. The temperature measurement error is derived as a root-mean-square-error on the absolute values of temperature recorded, using the data logging resolution of ±0.01 °C. The largest fraction is 0.066. A single curve fit is observable in the presented results and it is evident that the error fraction may be reduced by increasing $\dot{Q}_{surf}$, achieved by using a greater current magnitude or reducing T_{con}. However, given the behaviour of each individual cell model is unique, it would be limiting to propose a minimum current magnitude or desirable low temperature that should be used to find a cell model's CCC_{surf}. The determined CCC_{ERR} can be used as a universal measure of the error

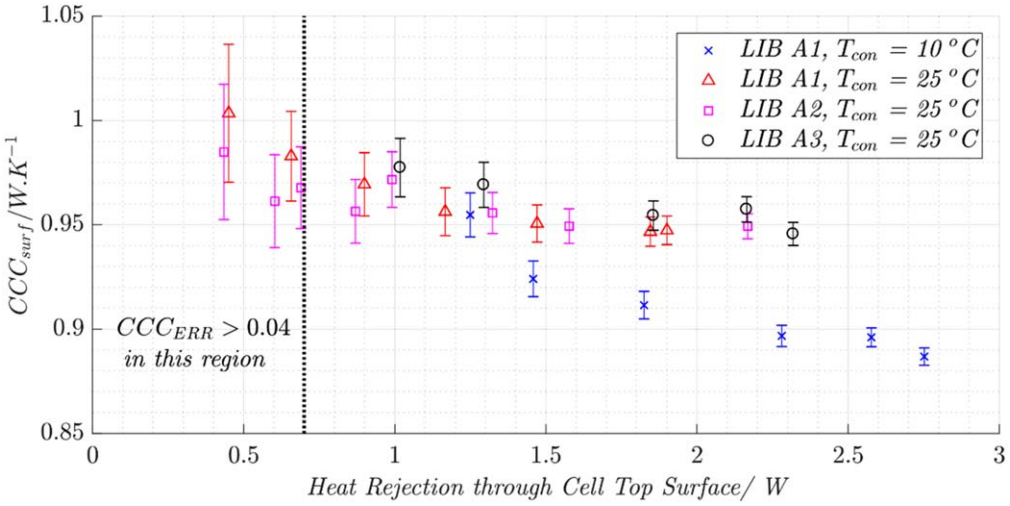

Figure 6. The derived CCC_{surf} for all tests on LIB A, plotted against the rate of heat rejection through the cell's top surface. The error due to the precision of the temperature measurement is included for all results. Also included is the threshold $\dot{Q}_{surf}$ value = 0.7 W, below which $CCC_{ERR} > 0.04$.

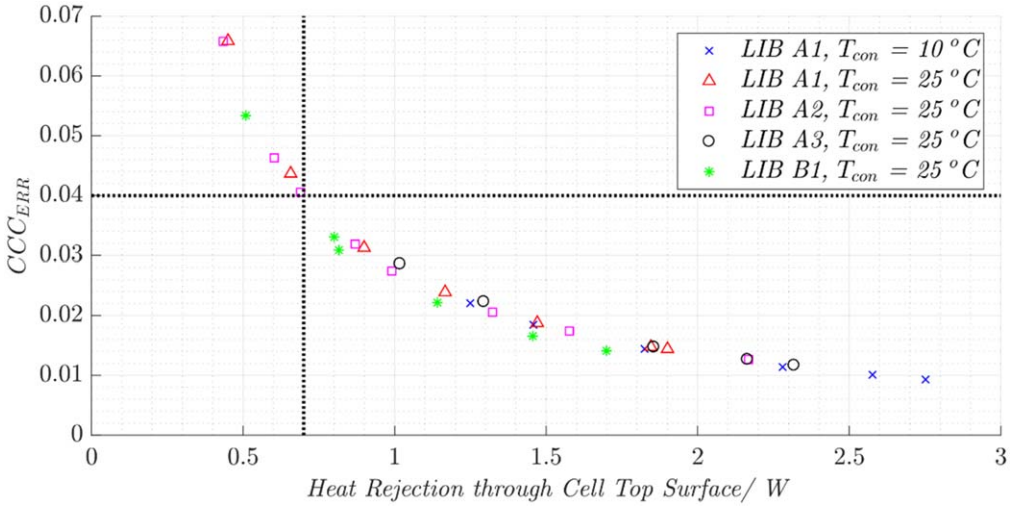

Figure 7. CCC_{ERR} for all tests, plotted against the rate of heat rejection through the cell's top surface. The proposed condition for acceptable error, $CCC_{ERR} < 0.04$, is included. $CCC_{ERR} < 0.04$ is directly to the experimental threshold for $\dot{Q}_{surf} = 0.7$ W. This condition is also included.

inherent to any single test on any given cell model. Therefore, a limit is proposed on Fig. 7, that $CCC_{ERR} < 0.04$ in order for the experimental error from the test to be sufficiently low to conduct meaningful analysis on the results. This proposal is carried forward in the present investigation, only results meeting the criterion are included in the remaining discussion.

From Fig. 7, it is evident that the criterion $CCC_{ERR} < 0.04$ is met when $\dot{Q}_{surf} > 0.7$ W. This is the threshold value for the experimental apparatus, and a vertical line is now included, marking the boundary between the acceptable and unacceptable regions, on Fig. 6 and Fig. 7.

Figure 8 plots the calculated CCC_{surf} values against the cell $\dot{Q}_{gen}$ for all valid tests on LIB A. As well as varying the magnitude of current in the pulsing profile, the controlled boundary temperature was dropped for the series of tests on LIB A1 to increase the impedance of the cell, and therefore $\dot{Q}_{gen}$, for a given current magnitude. Linear least square lines of best fit for each of the four datasets are also presented.

There is evident correlation between CCC_{surf} and $\dot{Q}_{gen}$. The lines of best fit have an average gradient of -0.0241. Across the sampled $\dot{Q}_{gen}$ range (0.58 W—3.23 W), this gradient predicts a 6.39% reduction in the outputted CCC_{surf}. This is a small error, attributable to the varying thermal behaviour of the current carrying copper wires, and therefore unaccounted for in the previous error analysis. The copper wires, connecting the cell to the battery cycler, are essential to the rigs functionality and may not be avoided. However, the error induced by them is in-line with that reported in published work surrounding the use of adiabatic testing to approximate a cell's specific heat capacity or rate of heat generation.[12,48,49]

Measures taken allowed both tabs to be included in the data processing that yielded results for $\dot{Q}_{gen}$. However, the varying degrees to which heat was rejected through the tabs, rather than the cells' top surface, affect the derived CCC_{surf}. The bottom of the cell reaches a higher temperature, and therefore it is reasonable to assume a greater portion of the heat rejected through the tabs is lost from the layers close to the bottom of the electrode-stack. This would reduce heat flux passing through the electrode-stack to the top surface of the cell, and consequently reduce ΔT_{cell} for a given $\dot{Q}_{gen}$. Further, in cases where the clamp sub-assembly reaches a higher temperature than the considered cell end, and consequently heat is added to the cell through the tab thermal pathways, the same assumption would suggest a greater portion of heat is added to the cooler layers: those closer to the top of the electrode-stack. This heat must be rejected through the top surface of the cell, conducting through the brass fins. Therefore, the reported $\dot{Q}_{surf}$ would in this case increase, whilst the heat flux from the bottom to the top of the electrode-stack, and therefore ΔT_{cell}, would be comparatively unaffected.

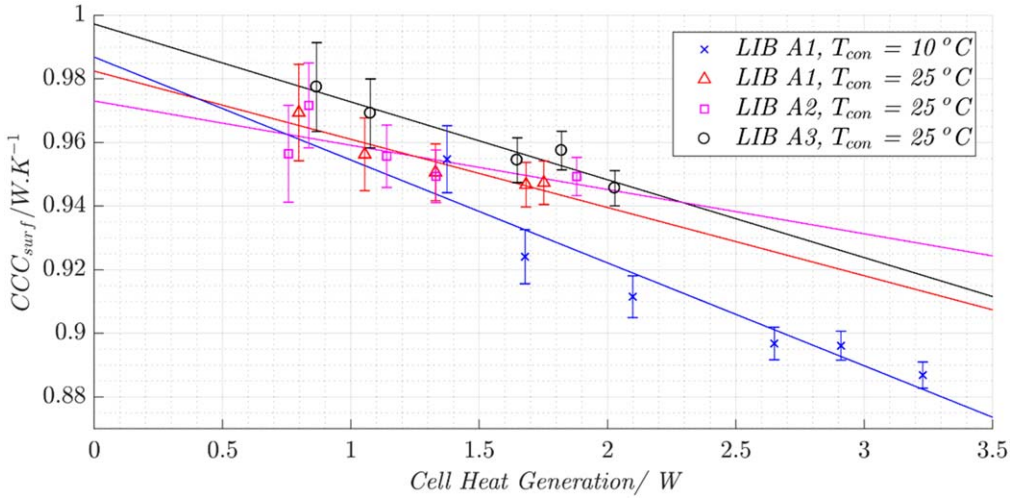

Figure 8. The derived CCC_{surf} for all tests on LIB A where the condition $CCC_{ERR} < 0.04$ is met, plotted against the rate of heat generation in the cell. A linear least square line of best fit is included for each dataset.

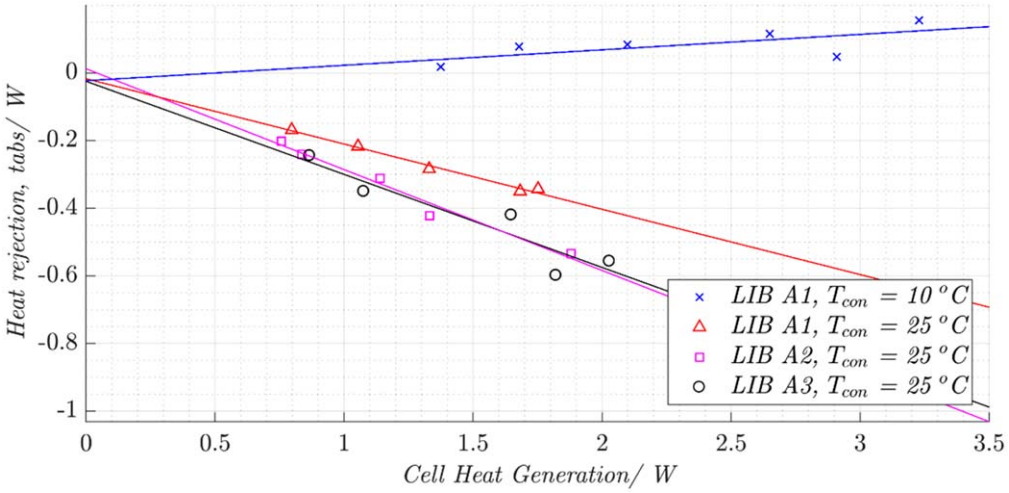

Figure 9. The rate of heat rejection through the cell tabs for all tests on LIB A where the condition $CCC_{ERR} < 0.04$, plotted against the rate of heat generation in the cell. A linear least square line of best fit is included for each dataset.

To demonstrate this phenomenon, this prediction is graphically displayed in Fig. 9, which plots the calculated $\dot{Q}_{tabs}$ ($\dot{Q}_{tabs} = \dot{Q}_{neg} + \dot{Q}_{pos}$) for each of the four LIB A datasets against $\dot{Q}_{gen}$. Regarding $T_{con} = 25$ °C tests, the gradient of the least square lines of best fit varies from one dataset to the next. This is caused by and represents variation in the degree of ohmic heating in the clamp subassembly and cables connecting the cell to the cell cycler, $\dot{Q}_{clamps} + \dot{Q}_{cables}$, and therefore the magnitude and direction of conductive heat transfer along the cables. $\dot{Q}_{clamps}$ and $\dot{Q}_{cables}$ were proportional to I_{pulse}^2 and the internal resistance of the clamp subassembly and cables, R_{clamps} and R_{cables}, respectively. Whilst measures were taken to achieve repeatable R_{clamps} values during experimental setup, the values measured prior to each test ranged from 0.101 mΩ to 0.197 mΩ at the positive clamp, and from 0.126 mΩ to 0.176 mΩ at the negative clamp. Therefore, qualitatively, for tests where $T_{con} = 25$ °C, heat was passed into the cell from the clamp subassemblies, whilst heat was rejected from the cell to the clamp subassemblies in tests where $T_{con} = 10$ °C.

The origin of Fig. 9 represents the definitive case where $I_{pulse} = 0$ A, and therefore $\dot{Q}_{gen} = 0$ W and $\dot{Q}_{clamps} + \dot{Q}_{cables} = 0$ W and all errors will also equal zero. Extrapolation of each line of best fit to the y-axis intercept axis ($\dot{Q}_{gen} = 0$ W) finds a point close to this axis origin ($\dot{Q}_{tabs} = 0$ W). This validates the argument that R_{clamps} variance is responsible for the varying fitted gradients: when R_{clamp} has no effect, i.e. when $I_{pulse} = 0$ A, each dataset converges on the point $\dot{Q}_{clamps} + \dot{Q}_{cables} = 0$ W, $\dot{Q}_{gen} = 0$ W.

Cell cooling coefficient determination.—The CCC derivation process has been shown to be reliable, and repeatable for multiple cell setups. Further, CCC_{surf} has been shown to be minimally affected by the cell temperature. Limitations have been highlighted with the apparatus, regarding variance in R_{clamps}. However, the error created by this, observable in the variability of derived CCC_{surf} from each individual test, has been presented as a solvable property through converging lines of best fit. The same methodology is proposed to derive a true CCC_{surf} value for each dataset (i.e. when the variability due to changing ohmic heating in the clamp-subassemblies and copper wire is eliminated). Returning to Fig. 9, and extrapolating the lines of best fit to the y-axis intercept, a true CCC_{surf} value can be found for each dataset. These are summarised in Table IV. The same methodology has also been applied to the LIB B1 dataset. The standard deviation of the four derived true CCC_{surf} values (for the four LIB A datasets) is 0.0066 and the maximum range within the values is just 1.42%. The variation in true CCC_{surf} is smaller than the TC error inherent to the apparatus setup. Therefore, the CCC_{surf} at the y-axis intercept is used for the following discussion.

Table IV. The theoretically derived CCC_{surf} value for each dataset, calculated for an instance where no current is being passed through the test cell.

Dataset	CCC_{surf}/ W.K^{-1}
LIB A1, $T_{con} = 10$ °C	0.987
LIB A1, $T_{con} = 25$ °C	0.983
LIB A2, $T_{con} = 25$ °C	0.973
LIB A3, $T_{con} = 25$ °C	0.997
LIB B1, $T_{con} = 25$ °C	1.907

Cell performance comparison.—Cell thermal performance may be compared using well established metrics such as thermal conductance, as is done below. However, the analysis in following paragraphs highlights the shortfalls of such established thermal performance metrics when they are applied within the electrochemical research field. Electrochemical devices, lithium-ion cells and beyond, are unique in their manner of heat generation, and thus a thermal performance metric devised specifically for them is absolutely essential as the field continues to expand at an enormous rate.

The thermal and geometric parameters affecting surface cooling performance for both cell models were summarised in Table I and Table II. From these, a thermal conductance for each cell ($C_{th\ LIB\ i}$) can be calculated through Eq. 13, where A and x are the cross-sectional area and thickness of the cell respectively. $C_{th\ LIB\ A} = 0.379$ W.K^{-1} and $C_{th\ LIB\ B} = 0.792$ W.K^{-1}.

$$C_{th} = \frac{k_{eff} A}{x} \quad [13]$$

The thermal conductance provides a means for a quantitative comparison of the thermal performance of the two cells. This metric states that LIB B outperforms LIB A by 108.7%. However, this comparison technique relies on unjustifiable assumptions: the effect of the conductive pouch cell material that provides a thermal pathway from one surface of the cell to the other is ignored and the thermal resistance of each interface within the electrode-stack is considered to be negligible.

The thermal conductance comparison is also not representative of an electrochemical device in operation. A thermal conductance can only be resolved with a singular characteristic length, and in this case the cell thickness was used. However, this therefore describes a situation where all heat is conducted from one surface of the cell to the other. In reality, any electrochemical device will generate heat, nonuniformly, throughout its volume due to both the reversible and

Table V. The derived CCC_{surf} and CCC_{tabs} for LIB A and LIB B.

	CCC_{surf}/ W.K^{-1}	CCC_{tabs}/ W.K^{-1}	Max. continuous discharge rate/ A.(Ah)$^{-1}$	Capacity/ Ah
LIB A	0.985	0.332	30	5
LIB B	1.907	0.204	5	7.5

irreversible processes at the pore-scale in the active materials; entropy change associated with material phase changes, transport of charge and species in the solid and electrolyte phases and charge-transfer reactions at the interphase. Finally, this comparison was only possible because of previous extensive work focussing on the composition, volumetric fraction and exact properties of the materials making up the cell, specific making up the electrode-stack. Without this information, it would have been impossible to derive k_{eff} for either cell.

The CCC_{surf} values for LIB A and LIB B are presented in Table V. They provide an alternative method to quantitatively compare the thermal performance of two geometrically dissimilar pouch cells. The method does not require the unjustifiable assumptions essential to the thermal conductance example set out above, nor does it require the characteristic length approximation. Finally, the comparison is conducted empirically, hence no prior knowledge of the cells' compositions is necessary. Although dimensionally similar to thermal conductance, a CCC is a thermal property specific to a certain thermal management method and specific to a lithium-ion cell in operation. Therefore, a CCC states a far greater magnitude of heat rate may be achieved through the cooled surface of a pouch cell for a given thermal gradient. $C_{th\ LIB\ A}$ is 38.5% of $CCC_{surf\ LIB\ A}$ and $C_{th\ LIB\ B}$ is 41.5% of $CCC_{surf\ LIB\ B}$. The fact that a lithium-ion cell in operation generates heat throughout its volume is predicted to be the dominant factor in the considerable difference between the calculated thermal conductances and the measured CCC values. However, other assumptions and approximations detailed must have an effect to an unknown degree.

In previous work, LIB A was shown to outperform LIB B for tab cooling by 62.7%. In the present work LIB B is shown to outperform LIB A for surface cooling by 93.4%. This comparative benefit encompasses all the individual cell characteristics discussed in this study into two simple measures for thermal performance. The proposed experimental and analytical approach enables the determination of a true measure for any pouch cell's capability to reject heat from a single surface, without modelling the complex and coupled cell parameters alongside assumptions that are not justified. Demonstrably, CCC_{surf} is a valuable tool for cell designers to optimise cell design towards the best thermal performance for particular applications. Further, it provides pack engineers with a simple measure to assess the appropriateness of a given pouch cell for an application.

Cooling method comparison.—For both cells, surface cooling is the more effective method for removing heat, for a given thermal gradient. For LIB A the reduction in cell-wide thermal gradient, ΔT_{cell}, achieved through single surface cooling is 66.3% and for LIB B would be 89.3%. Surface cooling therefore appears to be highly beneficial, clearly optimal for bulk heat removal, and this is in-line with industry trends. However, this is not the only consideration, the magnitude and direction of the thermal gradients and where they might be concentrated is significant.

Tab cooling for LIB A actually only induces a modest thermal gradient in the plane of the layers[31] as recent work has demonstrated the thermal gradient is concentrated in the region of the current collector to tab connection region and is caused by a significant reduction in cross sectional area of thermally conductive material. Therefore, despite a hotter cell, there is less layer-to-layer impedance variation, current inhomogeneities and LIB A has the smallest difference in temperature between the hottest and coldest regions of the actual stack region for tab cooling.[20,37] In contrast, surface cooling generates significant thermal gradients in a direction normal to the layer-plane within the stack region, and therefore large impedance variation between layers, significant current inhomogeneities, the largest differences in temperature between the hottest and coldest regions of the stack, and accelerated degradation.[20,37,45] This is because the stack region has anisotropic thermal properties: the thermal conductivity in the direction relevant to surface cooling is at least an order of magnitude lower than that for tab cooling.[50]

Previous studies have investigated the consequence of the thermal gradients induced by either tab or surface cooling.[20] Degradation is dramatically reduced: by 67% in the case of LIB A under aggressive cycling conditions. Recent work has also shown that if the thermal bottleneck in the tab region can be opened up by increasing the tab thickness and thus the cross-sectional area of the thermally conductive material, then tab cooling rates could approach those of surface cooling.[51]

Enhancing the cell cooling coefficient.—CCC_{surf} may be enhanced for a given cell through redesign. As demonstrated qualitatively, the thermal conductivity of every material contained within the electrode-stack has an impact on the temperature gradient, from the hot surface to the cooled surface. Therefore, it stands to reason that by improving the thermal conductivity of any present material will improve the CCC_{surf} for a given cell. ΔT_{cell} can be considered as a global quantity that can be broken down as a sum of the temperature gradient across each material in the electrode-stack. Take first ΔT_{CCneg}, the temperature gradient across each negative current collector (which is in almost all lithium-ion cell). Table I highlights the excellent thermal conductivity of copper (398 W.m^{-1}K^{-1}), and therefore ΔT_{CCneg} will make up a very small portion of ΔT_{cell}. Instead, evaluate $\Delta T_{cathode}$, the temperature gradient across every cathode layer in the electrode-stack. The cathode material for LIB A and LIB B has a very low thermal conductivity (1.04 W.m^{-1}K^{-1} and 0.44 W.m^{-1}K^{-1}), and therefore a large portion of ΔT_{cell} is found in $\Delta T_{cathode}$. Enhancing the thermal conductivity of the cathode (and anode, and separator) would have considerable tangible benefits on the magnitude of the cell's CCC_{surf}.

In reality, the proposals set out above may be unrealistic. The cell's active materials are optimised for electrochemical performance, not heat rejection. CCC_{surf} may also be enhanced for a given cell chemistry by reducing the thickness of the cell design, and thus reducing the average distance from the site of heat generation within the electrode-stack, to the cooled surface. This same benefit may be realised by the cell user through applying thermal management to both cell surfaces.

It is more realistic to enhance the CCC_{tabs} magnitude for a given cell chemistry and geometry. Published findings highlight the tab region of a pouch cell as a considerable thermal bottleneck within the tab cooling heat rejection pathway.[51] Typically, a pouch cell has tabs with thickness of 0.2–0.3 mm. Proposals are outlined to considerably increase the thickness of a given cell's tabs, to 1.5 mm. Validated numerical models conclude that for certain commercial pouch cells, redesign in this manner would make tab cooling the optimal cooling strategy, where at present surface cooling is the only viable thermal management method.

Application.—The CCC can improve the process for battery pack design by summarising thermal performance into a globalised metric

Table VI. Comparison of LIB A and LIB B, as well as cooling method, to determine suitability for application in an example battery pack.

Cooling method	Cell	Cell heat rate ($\dot{Q}_{gen}$) / W	$\Delta T_{cell\ max\ to\ surf}$/ °C	Maximum cooled surface temperature/ °C
Tab cooling	**LIB A**	4.97	14.97	25.03
	LIB B	8.28	40.59	-0.59
Surface cooling	**LIB A**	4.97	5.05	34.95
	LIB B	8.28	4.34	35.66

which allows for comparison of geometrically and thermally dissimilar cells. A basic example is set out below. It is not possible to propose an entirely realistic battery pack design procedure without diluting the key content of the present study. Thus, this example has been kept very simple in order to concisely demonstrate an instance where the CCC metric may be of value to industry.

A 15 Ah battery pack is required to operate entirely below 40 °C in ambient conditions of 20 °C, and must be capable of a continuous 4C discharge. The pack is to be designed to use either LIB A (three cells would be required) or LIB B (two cells would be required), and their key performance characteristics, the conventional capacity and maximum continuous discharge rate alongside CCC_{surf} and CCC_{tabs}, are summarised in Table V. The average rate of heat generation, $\dot{Q}_{gen}$, for LIB A and LIB B for a 4C discharge is 4.97 W and 8.28 W respectively.[42]

In the previous investigation, LIB B's incapability to be tab cooled for this application was found through calculations using CCC_{tabs}. It was demonstrated that the tabs must be kept almost 41 °C below the cell's maximum temperature, $\Delta T_{cell\ max\ to\ tabs}$, during operation. This would result in sub-zero coolant temperatures. LIB A, meanwhile, was a suitable choice for the tab cooled application. Maximum tab temperature was calculated to be 25 °C (i.e. $\Delta T_{cell\ max\ to\ tabs} = 15$ °C). These results are summarised in the first two rows of Table VI.

Considering instead a pack layout where each cell may be cooled on one surface, $\Delta T_{cell\ max\ to\ surf}$ is calculated through Eq. 14.

$$\Delta T_{cell\ \max\ to\ tabs} = \frac{\dot{Q}_{gen}}{CCC_{1\ surf,\ 0}} \qquad [14]$$

Therefore, for LIB A:

$$\Delta T_{cell\ \max\ to\ surf} = \frac{4.97}{0.985} = 5.05\ ^{\circ}\mathrm{C}$$

and for LIB B:

$$\Delta T_{cell\ \max\ to\ surf} = \frac{8.28}{1.907} = 4.34\ ^{\circ}\mathrm{C}$$

These results are summarised in rows 3 and 4 of Table VI. Required cooled surface temperatures are similar, representing the fact that even though LIB B generates more heat, it is counteracted by its better CCC_{surf} value. For the given application, surface cooling is the only suitable thermal management method for LIB B.

The following academic example demonstrates that LIB A may be either surface cooled or tab cooled for this hypothetical battery pack. For simplicity, it is assumed that the battery pack designer is set on using LIB A, with an optimum temperature of 25 °C, but has a decision to make regarding the implementation of either tab or surface cooling. In this case, the benefits of tab cooling (reduced degradation and extended pack lifetime) must be weighed against the potential for the pack to operate up to 15 °C above the optimum. This is compared to surface cooling, where the pack will always operate within 5 °C of its optimum. Whilst this example is not entirely representative of design methodologies that would be found in the automotive industry, it is able to simply demonstrate the value of the CCC metric as an additional tool to help with pack optimisation.

Conclusions

The surface Cell Cooling Coefficient is introduced, and a standardised method to quantify the thermal gradient required, across the thickness of a pouch cell, to a remove a unit of heat, generated within the cell, through the cell surface. The surface Cell Cooling Coefficient is empirically derived and a constant for a given cell model, regardless of operational parameters.

An industry standard to universally quantify the thermal management capability of any lithium-ion battery fits alongside the existing measures used to quantify power and energy density that may be found on any cell datasheet. The CCC metric will be of significant value across the lithium-ion battery industry. Battery pack designers gain a valuable tool enabling cell to cell comparison in order to select the most appropriate cell model for an application. CCC_{surf} and CCC_{tabs} should be employed in the early stages of battery pack design, to compare different thermal management methods for any cell and any operational conditions. An example of such a process is given in this study. CCC_{surf}, is shown to be a singular value for a given cell model, with a maximum variance of 1.82% for the full dataset of tests on LIB A. The experimental procedure has been shown to output repeatable results as the test conditions, magnitude of current passing through the cell and control temperature, are varied from test to test. The effect of T_{con} variation on the electrical resistance of, and therefore ohmic heat generation within, the clamp sub-assembly has been analysed. A methodology to compensate for this error was also presented.

The empirical CCC_{surf} metric has been devised specifically for electrochemical devices that generate their own heat. Therefore, it is unique when compared to conventional thermal performance metrics such as thermal conductance or the Biot number. Both are very difficult to parameterise due to the number of fundamental material properties and cell parameters required, and are dimensionally unable to characterise the nonuniform heat generation throughout the volume of any operational electrochemical device. The electrochemical research field is a fundamental component of the growing battery industry, and lithium-ion cell thermal management is a critical barrier to the widescale uptake of battery technology for the automotive sector and beyond. Therefore, a metric devised to improve understanding of lithium-ion cell temperature and internal temperature gradients, when in operation, will be a useful tool for fundamental electrochemical researchers and battery pack designers alike.

Uptake of the CCC will evolve the current battery design ethos. At present, cell manufacturers optimise energy density at the expense of heat rejection capability because energy density is the sole metric used to down-select for an application. A greater awareness to thermal performance, generated through a CCC dataset, will highlight this shortfall. In practice, it is anticipated that cells designed around the CCC will revolutionise battery pack design, leading to longer pack lifetimes, and greater accessible capacity.

Acknowledgments

This work was supported by the Faraday Institution (grant number EP/S003053/1, FIRG003), the Innovate UK THT project (grant number 105297), the Innovate UK BATMAN project (grant number 104180), the Innovate UK CoRuBa project (133369), and the EPSRC TRENDS project (grant number EP/R020973/1).

References

1. G. Zubi, R. Dufo-lópez, M. Carvalho, and G. Pasaoglu, *Renew. Sustain. Energy Rev.*, **89**, 292 (2018).
2. International Energy Agency, *World Energy Outlook 2018*, IEA, Paris (2018).
3. P. K. Nayak, L. Yang, W. Brehm, and P. Adelhelm, *Angew. Chem. Int. Ed.*, **57**, 102 (2018).
4. T. M. Bandhauer, S. Garimella, and T. F. Fuller, *J. Electrochem. Soc.*, **158**, R1 (2011).
5. K. Onda, H. Kameyama, T. Hanamoto, and K. Ito, *J. Electrochem. Soc.*, **150**, A285 (2003).
6. S. J. Bazinski and X. Wang, *J. Power Sources*, **305**, 97 (2016).
7. D. Bernardi, *J. Electrochem. Soc.*, **132**, 5 (1985).
8. L. Rao, *J. Electrochem. Soc.*, **144**, 2697 (1997).
9. C. Heubner, M. Schneider, C. Lämmel, and A. Michaelis, *Electrochim. Acta*, **186**, 404 (2015).
10. A. Nazari and S. Farhad, *Appl. Therm. Eng.*, **125**, 1501 (2017).
11. H. Liu, Z. Wei, W. He, and J. Zhao, *Energy Convers. Manag.*, **150**, 304 (2017).
12. V. Srinivasan and C. Y. Wang, *J. Electrochem. Soc.*, **150**, A98 (2003).
13. X. Zhang, *Electrochim. Acta*, **56**, 1246 (2011).
14. M. Xiao and S. Y. Choe, *J. Power Sources*, **241**, 46 (2013).
15. Y. Lai, S. Du, L. Ai, L. Ai, and Y. Cheng, *Int. J. Hydrogen Energy*, **40**, 13039 (2015).
16. A. N. Mistry, H. R. Palle, and P. P. Mukherjee, *Appl. Phys. Lett.*, **114** (2019).
17. B. Y. Liaw et al., *J. Power Sources*, **119–121**, 874 (2003).
18. Y. Troxler et al., *J. Power Sources*, **247**, 1018 (2014).
19. M. Fleckenstein, O. Bohlen, M. A. Roscher, and B. Bäker, *J. Power Sources*, **196**, 4769 (2011).
20. I. A. Hunt, Y. Zhao, Y. Patel, and J. Offer, *J. Electrochem. Soc.*, **163**, A1846 (2016).
21. X. Feng et al., *Energy Storage Mater.*, **10**, 246 (2018).
22. X. Feng et al., *J. Power Sources*, **255**, 294 (2014).
23. K. J. Kelly, M. Mihalic, and M. Zolot, *17th Annu. Batter. Conf. Appl. Adv.*247 (2002).
24. J. Xun, R. Liu, and K. Jiao, *J. Power Sources*, **233**, 47 (2013).
25. Q. Wang, B. Jiang, B. Li, and Y. Yan, *Renew. Sustain. Energy Rev.*, **64**, 106 (2016).
26. R. Sabbah, R. Kizilel, J. R. Selman, and S. Al-Hallaj, *J. Power Sources*, **182**, 630 (2008).
27. Z. Ling, F. Wang, X. Fang, X. Gao, and Z. Zhang, *Appl. Energy*, **148**, 403 (2015).
28. Y. Deng et al., *Appl. Therm. Eng.*, **142**, 10 (2018).
29. D. Chen, J. Jiang, G. H. Kim, C. Yang, and A. Pesaran, *Appl. Therm. Eng.*, **94**, 846 (2016).
30. G. Xia, L. Cao, and G. Bi, *J. Power Sources*, **367**, 90 (2017).
31. H. Heimes et al., *18th IEEE Intersoc. Conf. Therm. Thermomechanical Phenom. Electron. Syst.* (2019).
32. L. W. Jin, P. S. Lee, X. X. Kong, Y. Fan, and S. K. Chou, *Appl. Energy*, **113**, 1786 (2014).
33. Y. Huo, Z. Rao, X. Liu, and J. Zhao, *Energy Convers. Manag.*, **89**, 387 (2015).
34. Y. Rogers and G. Mayhew, in *Work & Heat Transfer* (Pearson Education Limited, London, UK) 4th ed., p. 524 (1967).
35. D. Werner, A. Loges, D. J. Becker, and T. Wetzel, *J. Power Sources*, **364**, 72 (2017).
36. M. Fleckenstein, O. Bohlen, and B. Bäker, *World Electr. Veh. J.*, **5**, 322 (2012).
37. Y. Zhao, Y. Patel, T. Zhang, and G. J. Offer, *J. Electrochem. Soc.*, **165**, A3169 (2018).
38. D. H. Jeon and S. M. Baek, *Energy Convers. Manag.*, **52**, 2973 (2011).
39. W. B. Gu and C. Y. Wang, *J. Electrochem. Soc.*, **147**, 2910 (2000).
40. M. Ecker et al., *J. Electrochem. Soc.*, **162**, A1836 (2015).
41. P. Taheri and M. Bahrami, *SAE Int. J. Passeng. Cars - Electron. Electr. Syst.*, **5**, 164 (2012).
42. A. Hales et al., *J. Electrochem. Soc.*, **166**, A2383 (2019).
43. I. Hunt, "Thermal effects and management of lithium ion batteries for automotive applications." *Ph.D. Thesis*, Imperial College London (2017).
44. S. Du et al., *Appl. Therm. Eng.*, **121**, 501 (2017).
45. B. Wu et al., *J. Power Sources*, **243**, 544 (2013).
46. K. Shah et al., *J. Power Sources*, **271**, 262 (2014).
47. K. Shah et al., *J. Power Sources*, **258**, 374 (2014).
48. Y. Kobayashi et al., *J. Electrochem. Soc.*, **149**, A978 (2002).
49. E. Prada et al., *J. Electrochem. Soc.*, **159**, A1508 (2012).
50. S. J. Drake et al., *J. Power Sources*, **252**, 298 (2014).
51. Y. Zhao et al., *J. Electrochem. Soc.*, **166**, 2849 (2019).